Virtual screening for ultra-small NIR emitter with only two isolated hexatomic rings

Zuping Xiong[1,2,3], Jianyu Zhang[4], Lei Wang[1,2], Xiong Liu[1,2,3], Jing Zhi Sun[1,3], Haoke Zhang[1,2,3,*], Ben Zhong Tang[1,4,5,*]

[1]MOE Key Laboratory of Macromolecular Synthesis and Functionalization, Department of Polymer Science and Engineering, Zhejiang University, Hangzhou 310058, China

[2]Zhejiang-Israel Joint Laboratory of Self-Assembling Functional Materials, ZJU-Hangzhou Global Scientific and Technological Innovation Center, Zhejiang University, Hangzhou 311215, China

[3]Centre of Healthcare Materials, Shaoxing Institute, Zhejiang University, Shaoxing 312000, China

[4]Department of Chemistry, Hong Kong Branch of Chinese National Engineering Research Center for Tissue Restoration and Reconstruction, The Hong Kong University of Science and Technology, Hong Kong, 999077, China

[5]School of Science and Engineering, Shenzhen Institute of Aggregate Science and Technology, The Chinese University of Hong Kong, Shenzhen (CUHK-Shenzhen), Guangzhou 518172, China

Corresponding emails: zhanghaoke@zju.edu.cn (Haoke Zhang); tangbenz@cuhk.edu.cn (Ben Zhong Tang)

Abstract

Unlocking the potential of weak interactions to govern the electronic structure of organic molecules remains a significant challenge. This study constructs a quantitative relationship between conformations and strength of electronic through-space interactions (TSI) for tetraarylethanes (TAEs). To identify long-wavelength emitters, a sophisticated virtual screening is executed for TAE by constructing a TSI-based database. Consequently, an ultra-small emitter (*o*-2Md), distinguished by a highly concentrated *n*-electron configuration, is synthesized and shows a remarkable near-infrared (NIR) emission with a luminescence quantum yield of 25% and an emission wavelength extending beyond 800 nm. Notably, the o-2Md stands out as one of the smallest known organic NIR emitters, showcasing the robustness of *n-n* TSI in designing efficient emitters. This work not only systematically reveals the important role of weak interactions in manipulating the electronic structure at the single-molecule level but also provides a new platform, the TSI database, for designing advanced optoelectronic materials.

1

INTRODUCTION

In the realm of material science, weak interactions exert a significant influence on microscopic systems, shaping biomacromolecule conformations and molecular recognition[1,2]. For instance, three-dimensional conformations of biomacromolecules are maintained by weak interactions, and non-covalent interactions wield significant influence over molecular recognition, binding, and catalysis[3,4]. However, in material design, researchers often focus on strong interactions related to covalent bonds but overlook the potential and contribution of weak interactions. Around 1970, Hoffman advocated the famous concept of through-space interaction (TSI),[5] which found applications in NMR spectroscopy-based techniques,[6] single-molecule conductors,[7] and other fields. However, because most TSI-based non-conjugated emitters fail to demonstrate exceptional photophysical performance, they have been neglected for nearly half a century. As shown in Figure 1a, until 2017,[8] it was surprisingly discovered that through-space π-π interaction (π-π TSI) could also induce excellent solid-state fluorescence (i.e., blue emission) like traditional through-bond conjugated dyes. Thus, TSI-based emitters have begun to attract widespread attention.[9,10] However, over the next seven years, despite trying various methods to design different multiarylalkanes (e.g., introducing electron donors or acceptors,[11] altering the length of alkyl chains,[12] and adjusting the length of π-π TSI[13]), the emission wavelength of the best emitter in each work still does not exceed ~470 nm. This implies that the ability of π-π TSI to promote long-wavelength emission is limited under certain conditions. Noticeably, some recent studies[14,15] have also highlighted unusual clusteroluminescence of non-conjugated polymers with numerous heteroatoms in the aggregate state. Even though they mostly exhibit weak clusteroluminescence, it serves as evidence for demonstrating the existence of TSI based on electron delocalization among heteroatoms. In Figure 1b, using the cumulative effect of numerous heteroatoms, it is possible for the lone pairs to stably form other types of TSI (such as n-n/π TSI). However, the specific structures of these polymers are unclear, showing the uncertainty of the luminescent structure. Meanwhile, it is found that some special non-conjugated polymers with a large number of heteroatoms may exhibit longer-wavelength emissions (beyond 480 nm).[16-19] This implies that utilizing the weak interactions based on lone pairs has the potential to design emitters with long-wavelength emissions.

Nonetheless, improving the performance of these non-conjugated emitters, characterized by low quantum yield and short emission wavelengths, remains a challenge due to the yet unexplored factors regulating TSI. Consequently, the task of constructing structure-property relationships relevant to TSI-based materials is both daunting and desirable. Addressing this challenge holds the promise of advancing the development of high-performance optoelectronic materials,[19-23] making it a crucial avenue for exploration in the field. The construction of databases related to novel materials will significantly accelerate the exploration of unknown domains.[24] Thus, some researchers have gradually begun leveraging enormous computational resources to explore novel high-performance materials.[25] For the emerging research of TSI-based optoelectronic materials, making initial attempts at rationally constructing databases for the virtual screening of non-conjugated materials

2

with efficient photophysical performance is both innovative and urgently needed. However, we must confront the following questions: How to build a weak interaction database?

Furan (Ox), thiophene (Th), pyrrole (Pr), and pyridine (Py) possess different aromaticity and electronic structures due to the effect of diverse heteroatoms. As shown in Figure 1c, we primarily select the classic tetraarylethane (TAE) as a research model to design ideal non-conjugated emitters. Unlike the nearly flexible non-conjugated polymers, the TAE skeleton provides a certain rigid environment for heteroatoms, where the *n-n*/π TSI may induce new photophysical properties. Thirty-six TAE molecules were designed by systematically varying the types, numbers, and connecting positions of these heterocycles. Firstly, we conducted a rigorous conformational search for each molecule from tens of thousands of conformations. Then, time-dependent density functional theory (TD-DFT) calculations were performed for virtual screening based on the final candidates (i.e., conformational pool). The results of TSI database and four groups of experimental molecular design (Figure S1-S35) underscore the efficient role of lone pairs-based TSI (i.e., *n-n*/π TSI) in crafting effective non-conjugated luminophores. Moreover, we demonstrate the nature of *n-n* TSI and its significant role in improving photophysical performance compared with other types of TSI. Subsequently, an ultra-small NIR emitter (*o*-2Md) is identified, exhibiting a high luminescence quantum yield (25%) and an extended emission wavelength beyond 800 nm. Through contrastive analysis, these characteristics can be attributed to the influence of *n-n* TSI[26]. Compared to traditional large NIR emitters containing polycyclic aromatic structures[27-29] (typically exceeding 100 atoms), *o*-2Md stands out as one of the smallest organic NIR emitters known to date, comprising only 13 non-hydrogen atoms (molecular mass: only 172). This remarkable feat offers unprecedented inspiration for the design of efficient non-conjugated emitters.
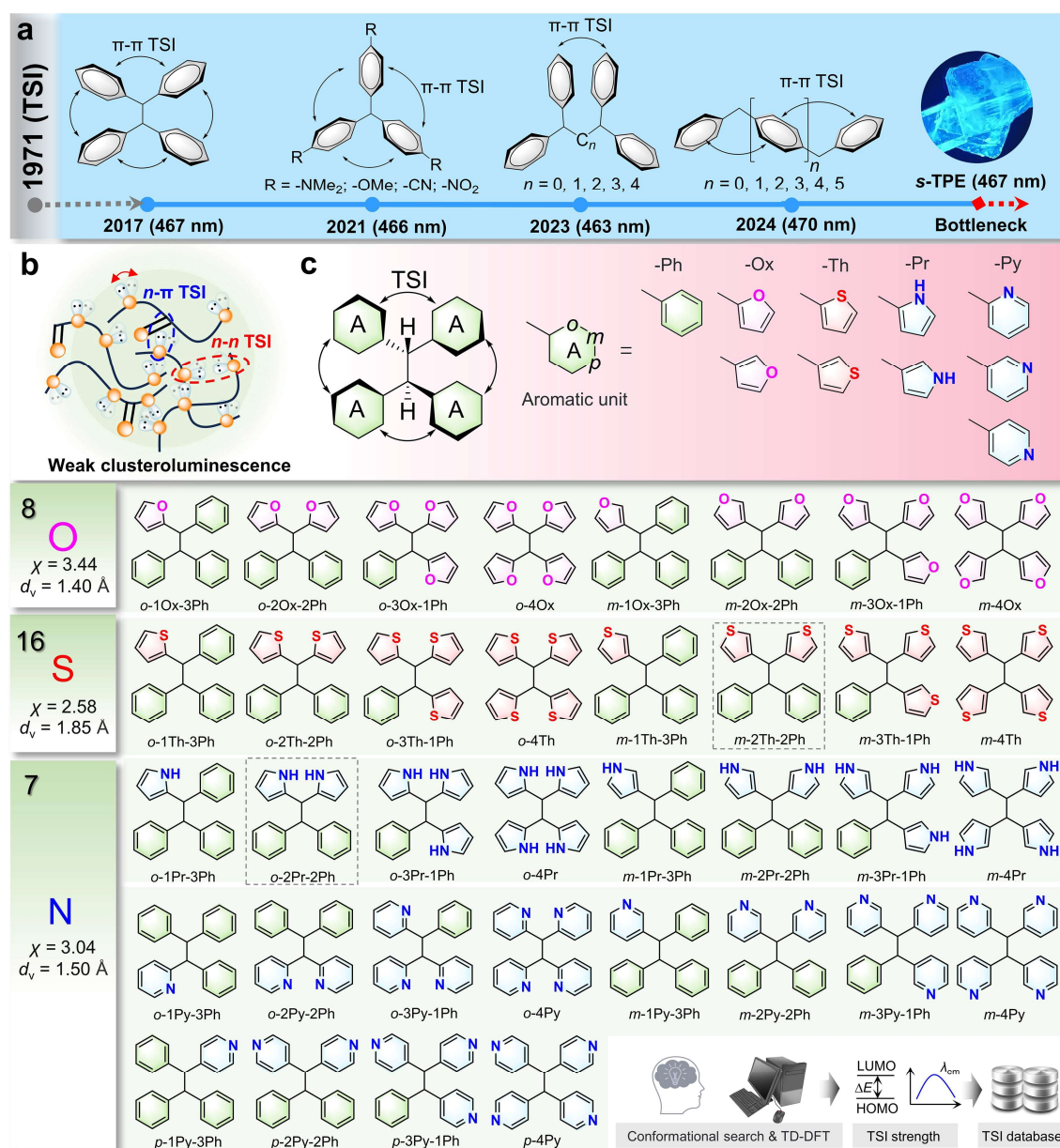
3

Figure 1. Virtual screening from thirty-six molecules

(**a**) The scientific history of designing non-conjugated emitters based on through-space interaction (TSI): Roald Hoffmann elaborated the TSI concept in 1971; the TSI-based blue emission of *s*-TPE (467 nm), TPM-CN (466 nm), C2-TPA (463 nm), and OPM[4] (470 nm) were reported in the seven years since 2017; The final image shows the blue fluorescence of the *s*-TPE crystal at 365 nm irradiation; These molecules are the best emitters in terms of photophysical performance for each study. (**b**) Weak clusteroluminescence induced by TSI among heteroatoms. (**c**) Construction of TSI database based on TD-DFT calculations of 36 tetraarylethanes. Note: electronegativity (χ); Van der Waals radius (d_v); ortho- (*o*-); meta- (*m*-); para- (*p*); the gray frame (conformational convergence fails); the causes of conformational convergence failure have been discussed in Supporting Information.

RESULTS AND DISCUSSION

Construction of the TSI database

4

Non-conjugated tetraphenylethane is a famous TSI model[8,12], and various heterocycles (Ox, Th, Pr, and Py) are severally introduced into tetraphenylethane to replace the benzene rings (Ph) as shown in Figure 1c. These heterocycles contain various types of heteroatoms with different electronegativity (χ) and van der Waals radius (d_v). For example, oxygen and nitrogen show higher χ (3.44 and 3.04, respectively) and smaller d_v (1.40 and 1.50 Å, respectively) than sulfur. Thus, when heteroatoms are introduced at different positions (*o*-, *m*- or *p*-) in a heterocyclic ring, the electronic structure is significantly affected. Meanwhile, changing the number of introduced heterocyclic rings (n) is also expected to directly affect the intramolecular TSI. Figure 1 lists 36 molecules with varying types, numbers, and connecting positions of heterocycles. For Ox-substituted TAE, there are 8 compounds based on the different numbers and connecting positions of heterocycles (i.e., *o*-1Ox-3Ph, *o*-2Ox-2Ph, *o*-3Ox-1Ph, *o*-4Ox, *m*-1Ox-3Ph, *m*-2Ox-2Ph, *m*-3Ox-1Ph, and *m*-4Ox). The same naming rules also apply to Th/Pr/Py-substituted TAE. However, there are 12 candidates for Py-substituted TAE because Py shows six-member heterocycles with three *N*-substituted positions (*o*-, *m*-, and *p*-).

It is worth noting that each molecule may have more than one reasonable conformation due to the different arrangements of heteroatoms. Therefore, we conducted rigorous conformational searches for each molecule. For example, using the Confab software, it was found that *o*-1Ox-3Ph has 7776 conformations. After the first round of screening all these conformations, 54 conformations remained. Further structural optimization was performed using the XTB with the GFN0-xTB method. A second round of conformational screening was conducted using the "isostat" tool, resulting in 8 conformations, from which the preferential conformation with the lowest energy was selected. This conformation, representing 79.11% of the Boltzmann distribution at 298.15 K, was used as the input structure for TD-DFT calculations. Similarly, after two rounds of conformational screening for *o*-2Ox-2Ph, it is found that there is no preferential conformation (the largest Boltzmann distribution is only 54.50% at 298.15 K). For these conformations obtained by the second screening, some extremely distorted and unreasonable structures are excluded based on chemical common sense. Finally, three conformations with the lowest energy (the order from lowest to highest: *o*-2Ox-2Ph(1), *o*-2Ox-2Ph(2), and *o*-2Ox-2Ph(3)) are chosen as the input for TD-DFT calculations. It is worth noting that the used TD-DFT method, B3LYP-D3(BJ)/6-31G(d,p), has been proven to be reasonable in Supporting Information. After the conformational search, 45 reasonable conformations were simulated to calculate their energy gap (ΔE) and emission wavelength (λ_{em}) based on their optimized excited-state geometries ($S_{1,min}$) (Figure S36-S38). These parameters, regarded as indicators of TSI strength, could be used to build a TSI database. All the detailed processes of conformational search and other calculational details for each molecule can be found in Supplementary Information.

Virtual screening based on the TSI database

The net distance of adjacent heteroatoms (Δd) calculated from the $S_{1,min}$ conformation is one of the determining factors for the strength of TSI in these TAE, $\Delta d = d - \sum d_v$, d: the measured distance between two adjacent heteroatoms, $\sum d_v$: the sum of van der Waals radii of two heteroatoms. A negative Δd represents that these two heteroatoms are in the range of the sum of their van der Waals radius values, suggesting a strong weak interaction. As shown in Figure 2a, the Δd is positive for most TAE, demonstrating a weak intramolecular TSI. However, *o*-4Ox(2), *o*-2Th-2Ph, *o*-3Th-1Ph(1-3), *o*-4Th(1 and 2), *o*-3Py-1Ph, and *o*-4Py(2 and 3) (Figure 2a) displayed the negative Δd (0.54 Å for O···O; -0.89~-1.86 Å for S···S; about -0.80 Å for N···N). This makes it possible for

5

heteroatoms to interact in terms of distance. Indeed, merely observing the Δd cannot determine the strength of interaction among heteroatoms. The molecular conformation and the types of heteroatoms also play crucial roles. For instance, sulfur atoms on Th are hardly capable of providing lone pairs (Figure S39), so even if they are very close, n-n TSI is impossible to exist. In addition, since the lone pairs have a specific orientation, an effective n-n TSI can only possibly exist when the lone pairs carried by heteroatoms are oriented appropriately. For better comparative analysis, Atoms-In-Molecules (AIM) analysis was performed for all conformations (Figure S40-S43), and the electron density (D) at bond critical points (BCPs) was used to measure the strength of TSI quantitatively.[30] Due to either the involvement of heteroatoms in hydrogen bonding (e.g., oxygen atoms in o-3Ox-1Ph(1) and o-4Ox(1)) or the significant distance between heteroatoms (e.g., oxygen atoms in m-4Ox), it is apparent that most heteroatoms cannot exhibit significant interactions with each other. Apparently, the formation of interactions between lone pairs and C-H competes with the formation of n-n/π TSI due to the limited number of lone pairs in small emitters. However, a BCP between the carbon and oxygen atoms ($D_{O \cdots C} = 0.017$) was identified in o-4Ox(2), suggesting the presence of n-π TSI (refer to Figure S40). Its calculated emission (400 nm) is the largest in the Ox-based TAEs. Thus, the TSI database also indicates that n-π TSI may induce a redshift in emission.[31,32]

BCPs between sulfur and carbon atoms were also observed in some Th-based TAE (Figure S41). However, this interaction is not related to lone pairs. It is evident from Figure S42 that the pyrrole ring lacks any excess lone pair electrons contributing to the formation of the BCP. Additionally, a BCP between nitrogen and carbon atoms ($D_{C \cdots N} = 0.011$) was detected in o-4Py(1), while BCPs between two nitrogen atoms ($D_{N \cdots N} = {\sim}0.050$) were identified in o-3Py-1Ph, o-4Py(2), and o-4Py(3) (Figure S43). This indicated that n-n TSI is significantly stronger than n-π TSI. It is worth noting that such strong interactions between adjacent lone pairs may induce smaller ΔE and longer-wavelength emissions, which is reflected in the TSI database. For example, o-4Py(3) exhibits the smallest ΔE (2.31 eV) and the longest λ_{em} (718 nm) (Figures 2b and 2c). Once the nitrogen atoms are placed in the para position of pyridine (p-4Py), the Δd (~2.76 Å) is too long to form TSI between N atoms. Large ΔE (4.78 eV) and short λ_{em} (360 nm) of p-4Py were predicted with poor luminescence properties. Thus, referring to the database, we can anticipate that the higher concentration of nitrogen atoms with reasonable substituted positions tends to trigger long-wavelength emissions (even NIR emission).
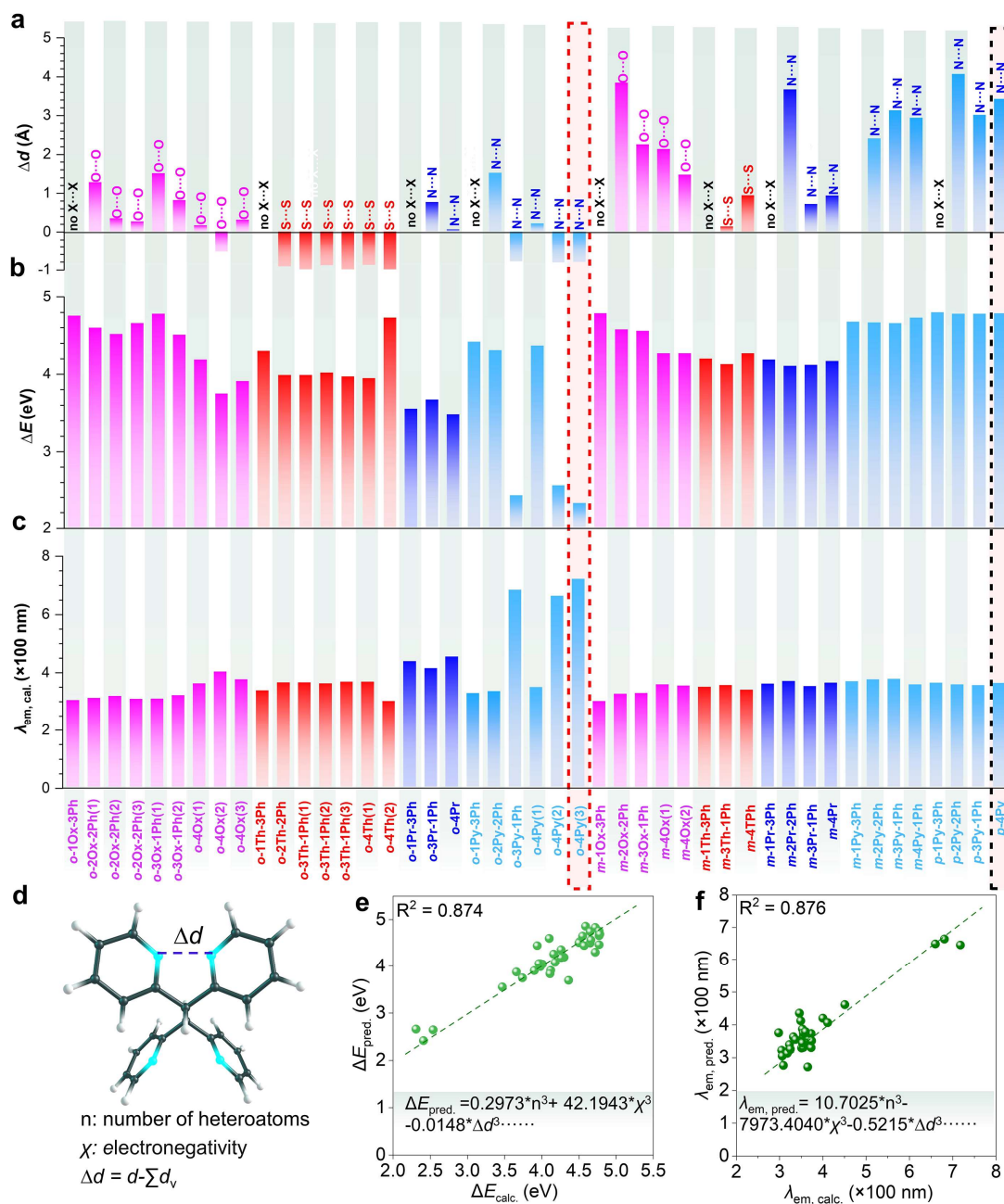
6

Figure 2. Through-space interaction database based on TD-DFT calculations.
(**a**) The calculated net distance (Δd) between two adjacent heteroatoms, $\Delta d = d - \sum d_v$, d: the measured distance between two adjacent heteroatoms, $\sum d_v$: the sum of van der Waals radii of two heteroatoms. (**b**) The calculated energy gap between the highest occupied molecular orbital and the lowest unoccupied molecular orbital. (**c**) The emission wavelengths ($\lambda_{em,\,cal.}$) calculated by TD-DFT. Note: all results are based on the optimized excited-state conformation ($S_{1,min}$). (**d**) Geometrical parameters of the computational model (Δd, n and χ as variables, and calculated ΔE and λ_{em} as dependent variables respectively). (**e-f**) The relationship between predicted values ($\Delta E_{calc.}/\lambda_{em,\,calc.}$) and calculated values ($\Delta E_{pred.}/\lambda_{em,\,pred.}$), the predicted values were achieved from the empirical equations inside panels e and f (the complete formula is available in Supporting Information).

Furthermore, it is pivotal to establish a structure-property relationship among molecular geometry,

TSI strength, and photophysical properties, which could guide the molecular design for TSI-based emitters. According to the above analysis, intramolecular heteroatom-involved TSI is closely related to χ, n, and Δd as shown in Figure 2d. Then we formulated two computational descriptors based on the identified independent variables. These descriptors[33] were utilized to explore the functional correlation between the calculated $\Delta E/\lambda_{em}$ and the aforementioned independent variables—namely, χ, n, and Δd. These two abbreviated formulas in Figures 2e and 2f suggest that χ, n, and Δd show a cubic relationship with ΔE and λ_{em}. Meanwhile, when the obtained formulas were used to predict the ΔE and λ_{em} based on these three independent variables, the predicted values were quite similar to the calculated ones, almost showing a linear relationship (Figures 2e and 2f). These results confirm the possibility of predicting TSI solely based on the chemical structure and molecular conformation.
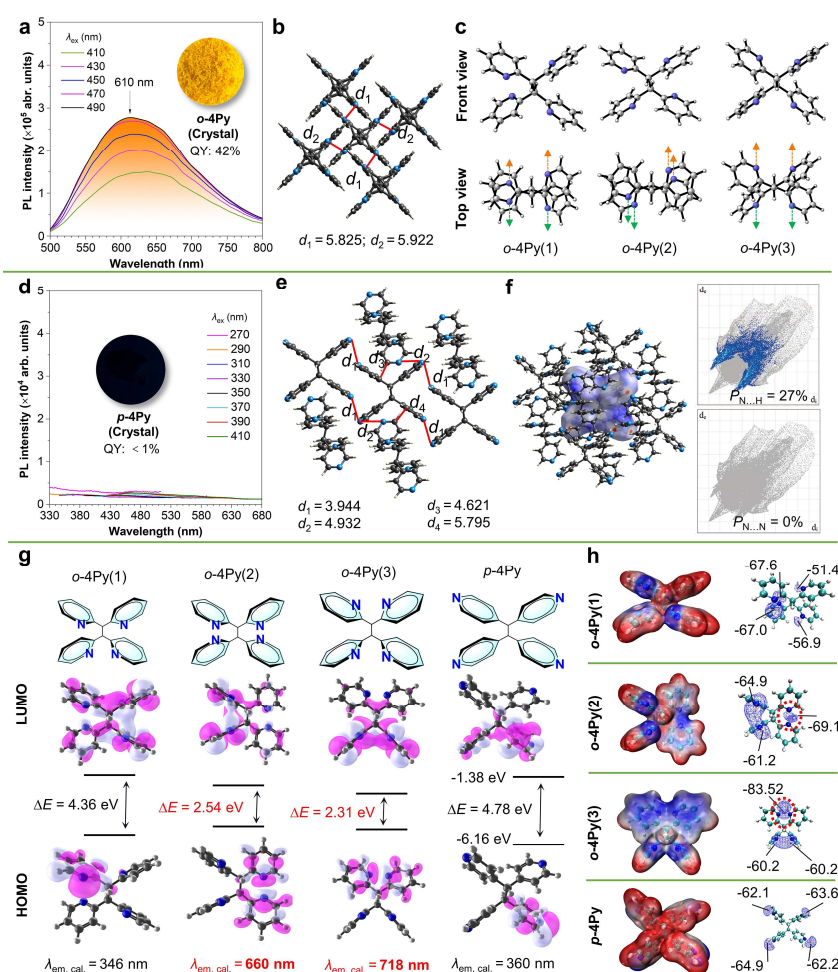

Figure 3. Effects of the substituted positions on photophysical properties.
(**a**) Excitation-dependent PL spectra and (**b**) crystal packing diagram of o-4Py(crystalline state). (**c**) 3 conformations of o-4Py are obtained by conformation search and DFT calculation (B3LYP-D3(BJ)/6-31G(d,p)), and arrows of different colors indicate the different orientations of N atoms in o-4Py(1-3). (**d**) Excitation-dependent PL spectra, (**e**) crystal packing diagram, (**f**) Hirshfeld surfaces and decomposed fingerprint plots of p-4Py (crystalline state). Note: the full fingerprints appear as gray shadows underneath decomposed plots, and the intermolecular N···H interaction is shown as a blue shadow; $P_{N\cdots H}$ and $P_{N\cdots N}$: proportion of nitrogen-hydrogen and nitrogen-nitrogen

8

intermolecular interaction to total intermolecular interaction. (**g**) Distribution of electron cloud and energy levels of the highest occupied molecular orbital (HOMO) and the lowest unoccupied molecular orbital (LUMO) for o-4Py(1), o-4Py(2), o-4Py(3) and p-4Py with 4 N atoms in different positions of the optimized excited-state conformation ($S_{1,min}$). (**h**) Electrostatic potential of o-4Py(1), o-4Py(2), o-4Py(3), and p-4Py, and the minimum value of ESP (V_{min}) is plotted to show the distributed region of lone pairs (blue grid area).

Proof scheme 1: Altering the substituted positions of heteroatoms

First, by synthesizing p-1Py-3Ph and m-1Py-3Ph, we demonstrate that only introducing a nitrogen atom into the s-TPE skeleton cannot effectively induce a redshift in luminescence (Figure S44). Then, to confirm the theoretical prediction, two emitters, o-4Py (positive control) and p-4Py (negative control), were synthesized (Figure S45). Their absorption spectra in both the solution and solid state exhibit the absorption maximum (λ_{ab}) at ~260 nm corresponding to isolated pyridine, confirming the non-conjugated nature (Figure S46). Meanwhile, their crystals can exhibit new λ_{ab} (~350 nm) corresponding to the $n \rightarrow \pi^*$ transition of pyridine. Figure 3a shows PL spectra of o-4Py crystal with different wavelengths of excitation (λ_{ex} from 410 to 490 nm), which shows a broad emission at 610 nm with a high fluorescence quantum yield (QY) of 42%. In Figure 3b, analysis of crystal packing for o-4Py eliminates the interference of intermolecular n-n TSI due to the overlong intermolecular N···N distance (~ 6.0 Å). Figure 3c shows the three different conformations obtained by the conformation searching and DFT calculation for o-4Py, and the disordered structure of the crystal structure confirms the presence of multiple conformations. This conformational distribution could explain the broad-band emission of o-4Py. However, the p-4Py crystal is almost non-luminescent (QY < 1%) under different λ_{ex} (from 270 to 410 nm) as shown in Figure 3d, and the excitation wavelength (λ_{ex}) of p-4Py (387 nm) is more blue-shifted than o-4Py (487 nm) (Figure S47a and S47b). Crystal packing of p-4Py (Figure 3e) shows that the shortest distances of N···N and C···C are also overlong (3.9 and 4.6 Å, respectively). The Hirshfeld partition analysis on p-4Py crystal shows that the proportion of N···N interactions (0%) is much smaller than that of N···H interactions (27%), confirming the absence of intermolecular n-n TSI (Figures 3f). The PL spectra of o-4Py in concentrated solution and low temperature also show brighter and longer-wavelength emission than p-4Py (Figures S47c and S47d, Figure S48). This suggests that the variations in electronic structure, caused by the different substituted positions of nitrogen atoms, can be effectively observed through spectroscopic analysis of the various states of these compounds.

Further analysis of the electronic structures in the TSI database can help elucidate the role of lone pairs in inducing long-wavelength emission. For o-4Py, when the N atoms were put on the same side, the resultant o-4Py(2) and o-4Py(3) showed narrow energy gap ΔE (2.54 and 2.31 eV, respectively) and long λ_{em} (660 and 718 nm, respectively). However, when all N atoms show a staggered orientation, o-4Py(1) exhibits large ΔE (4.36 eV) and ultraviolet emission (346 nm). The p-4Py also demonstrates poor TSI as o-4Py(1) (Figure 3g). Noticeably, the frontier molecular orbitals (FMOs, isovalue: 0.02) exhibit an asymmetric distribution in symmetric compounds. We exclude the occurrence of degenerate orbitals in LUMO+n and HOMO-n (Table S2), and the results of natural transition orbital (NTO, isovalue: 0.02) analysis are similar to those of FMO analysis (Figure S49) because the HOMO to LUMO transition is dominant for emission (Table S3). More specifically, the HOMOs are distributed in the region with strong TSI (e.g., n-n/π TSI), and this suggests that the electron in the area with higher electron density is more likely to be excited to the LUMOs. The TD-DFT spectra (Figure S50) show that the simulated emissions closely match

9

experimental results, ensuring the reliability of predictive performance based on this TSI database. The blue regions in the electrostatic potential (ESP, isovalue: 0.005) map can represent areas of high electron density, while the red regions indicate areas of low electron density. Thus, ESP demonstrates how the electron structure varies due to the conformational effects arising from the different positions of heteroatoms. Figure 3h shows the ESP of *o*-4Py(1-3) and *p*-4Py, indicating that placing N atoms close enough in the center will induce high electron density (blue area), such as *o*-4Py(2) and *o*-4Py(3). For *p*-4Py, due to the strong electronegativity of the N atom, 4 nitrogen atoms can attract electrons to the periphery, and then weaken the electron density at the molecular center (i.e., weaken the π-π TSI), thereby causing luminescence quenching. In the right panel of Figure 3h, the blue grid region (isovalue: -0.045) clearly illustrates the part of the molecule with the highest electron density.[34] Meanwhile, the minimum value of ESP (V_{min}) is also plotted to show the lone pair region inside molecules, and V_{min} in the lone pair region indicates the electron-rich character of the lone pair. It is worth noting that when lone pairs approach in a nearly head-to-head manner, they can form a more negative V_{min}, implying the presence of a stronger TSI. Meanwhile, by comparing the V_{min} produced by the different orientations of the lone pair electrons, it is confirmed that the formation of effective *n*-*n* TSI entails certain directional requirements for the lone pairs. For example, if the lone pairs of pyridine cannot effectively overlap (i.e., be similar to head-to-head type), their V_{min} ranges from -51.4 to -64.9 kcal/mol. However, some parts of *o*-4Py(2) and *o*-4Py(3) exhibit a head-to-head overlap of lone pairs (red-circled area), and they show larger V_{min} (-69.1 and -83.52, respectively).
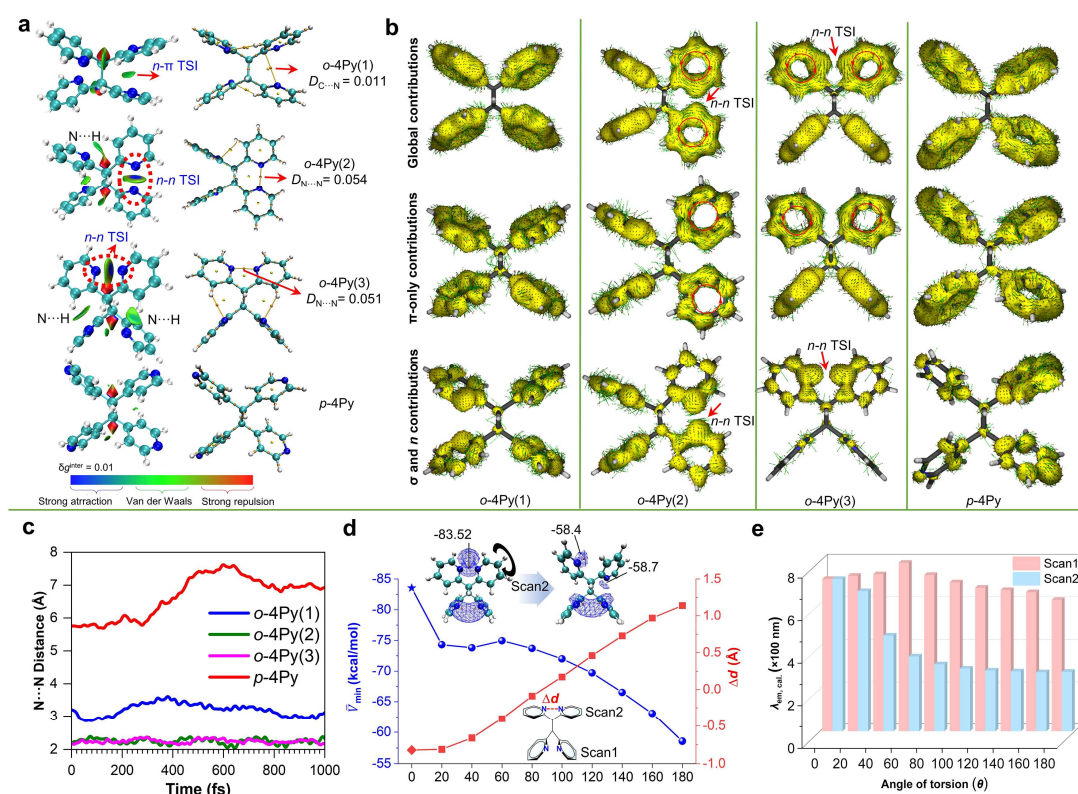

Figure 4. The nature and functions of *n*-*n* TSI.

(**a**) Hirshfeld partition of molecular density (IGMH) and AIM analysis of *o*-4Py(1-3) and *p*-4Py conformations ($S_{1,min}$). Note: the electron density (*D*) at the bond critical point (BCP) is used to

measure the strength of the weak interaction. (**b**) AICD isosurfaces of *o*-4Py(1-3) and *p*-4Py conformations ($S_{1,min}$). (**c**) Ab initio molecular dynamics (AIMD) analysis of these four conformations, and the distance between the two nearest N atoms is plotted over time (fs). (**d**) The change of the average values of V_{min} ($\overline{V}_{min}$) and Δd during the rigid scan 2 of *o*-4Py(3) in the excited state. The pyridine rings in the upper right corner and lower right corner were rotated in Scan 2 and Scan 1, respectively. (**e**) The change of $\lambda_{em, cal.}$ during the rigid scan 1 and scan 2 in the excited state.

Based on other methods, we further analyze the nature and functions of *n-n* TSI. Hirshfeld partition of molecular density (IGMH)[35] can directly reflect the strength of weak interactions based on the color difference (Figure 4a). This efficient *n-n* TSI can be reflected in the blue region between adjacent nitrogen atoms (red-circled area), indicating strong attraction between these two N atoms. It is worth noting that the strength of *n-n* TSI (blue-green parts) is much greater than the *n*-π TSI and even surpasses intramolecular N···H hydrogen bonds. These results are entirely consistent with the findings from our previous AIM analysis of the TSI database. Moreover, TSI can be displayed with AICD isosurfaces.[36] According to Figure 4b, AICD isosurfaces of *o*-4Py(1-3) and *p*-4Py are viewed for global contributions, π-only contributions, and sigma (σ)&*n* contributions to confirm the nature of *n-n* TSI. Their stereoscopic conformation can be referenced to the structure in Figure 4a. Here are the findings from the comparative analysis based on the AICD isosurfaces: 1) These TAEs only exhibit a diatropic ring current in the pyridine ring, indicating their non-conjugated nature. 2) By judging the thickness of the isosurface, sigma electrons do not exhibit overall delocalization but rather have significant localization in local space (near the C-C bonding region and around H atoms) compared to π electrons. 3) The lone pairs can exhibit significant electron delocalization near the N atoms. 4) When we exclude the contribution of π orbitals in the AICD isosurfaces of *o*-4Py(2) and *o*-4Py(3), new isosurfaces show that there exists a very distinct sigma-type *n-n* TSI between two head-to-head nitrogen atoms. 5) It is worth noting that compared with the AICD isosurface of the sigma bond (e.g., C-C bond and C-H bond), the isosurface corresponding to *n-n* TSI is relatively hypertrophic, showing its unique electron delocalization. The fourth and fifth points describe the nature of such *n-n* TSI, a significant discovery in chemistry. It is because we typically assume that electron donors repel each other when they approach, while electron donors and acceptors tend to attract each other. Here we have defined, for the first time, the nature of sigma-type *n-n* TSI which could be even stronger than hydrogen bonds in some cases. More specifically, sigma-type *n-n* TSI is a strong non-covalent bond formed in a head-to-head type by lone pairs, resembling the form of a sigma bond, but possessing electron delocalization properties similar to π bond. Moreover, it is worth mentioning that the region in sigma-type *n-n* TSI exhibits a very high electron density compared with common π/*n*-π TSI.

What is the function of such *n-n* TSI? Ab initio molecular dynamics (AIMD) is used to simulate the excited-state molecular dynamics of these four conformations (*o*-4Py(1-3) and *p*-4Py) in Figure 4c. Using the change of distance between the nearest two nitrogen atoms as a reference for measuring conformational motion, it is surprisingly found that *n-n* TSI in *o*-4Py(2) and *o*-4Py(3) can lock the molecular electronic structure like a covalent bond (Video S1-S4). This may explain why *o*-4Py crystals exhibit high solid-state QY. However, staggered lone pairs cannot stabilize the electron structure. To prove the quantitative relationship between the conformation and *n-n* TSI, the rigid scan of *o*-4Py(3) was performed based on its $S_{1,min}$ conformation. As shown in Figure 4d, *o*-4Py(3) exhibits an asymmetry conformation in which the upper two pyridine rings are almost coplanar and

11

their two N atoms align head to head. The lower two pyridine rings show almost perpendicular orientation. Scan 1 and scan 2 represent the rotation of one pyridine ring from lower and upper moieties, respectively, and this sigma-type n-n TSI can be broken by scan 2. The blue grid area represents the region with the highest electron density within the molecule, and Figure 4d shows that the electron density is significantly reduced in this region with disturbing the n-n TSI during scan 2. With increasing the torsion degree, the Δd of two N atoms in the upper two pyridine rings increased from -0.82 to 1.14 Å, and the average values of V_{min} ($\overline{V}_{min}$) underwent a dramatic change (from -83.52 to -58.6 kcal/mol). Meanwhile, the rotation of the lower pyridine (scan 1) cannot significantly affect the upper n-n TSI (Figure S51). According to Figure 4e, due to the distinct effects of these two scans on this sigma-type n-n TSI, there are different trends in calculated λ_{em} and ΔE versus the angle of torsion (Figures S52). More specifically, scan 2 significantly causes the blue shift of emission (from 718 to 282 nm), whereas scan 1 does not. It is demonstrated that the n-n TSI between the upper two pyridine rings with coplanar structure plays a dominant role in the λ_{em} and ΔE of o-4Py(3). The rigid scan of o-4Py(2) presents a similar result (Figures S53 and S54). As a result, it can be concluded that n-n TSI can stabilize the electronic structure and has a great ability to promote the redshift in emission.

Proof scheme 2: Changing the conformation to regulate Δd

To demonstrate the ability of lone pair-based TSI to promote emission, some non-conjugated derivatives outside the database were further synthesized to verify the reliability of the TSI database. *racemic-o*-2Py-2Ph and *meso*-o-2Py-2Ph were prepared and successfully isolated according to their different polarities (Figure 5a and Figure S55). In Figure 5b, *racemic -o*-2Py-2Ph crystal, two pyridine rings on the same side with short Δd of two N atoms, exhibits long-wavelength emission of 592 nm with QY of 11%. However, the *meso-o*-2Py-2Ph crystal only shows a weak blue emission of 402 nm (QY = 2%). Based on conformational search, both of these molecules have a dominant conformation. Then TD-DFT calculation is performed for *racemic-o*-2Py-2Ph and *meso-o*-2Py-2Ph. According to Figure 5b, the role of lone pairs differs in these two molecules due to conformational changes. It can be observed that the nitrogen atom of the upper pyridine interacts with the below pyridine ring in a manner resembling a perpendicular alignment (i.e., n-π TSI). Thus, ESP shows the high electron density in this interaction region (blue), and IGMH analysis also proves the existence of this strong n-π TSI. However, in *meso-o*-2Py-2Ph, the region near the nitrogen atom accumulates a significant number of electrons, yet the N atom participates in the formation of hydrogen bonds. It can be confirmed by the IGMH method because there are green fragments between C-H and N atoms. Therefore, there is no intramolecular n-n/π TSI in *meso*-o-2Py-2Ph. Here we verified the inverse relationship between Δd and λ_{em} by altering the conformation.
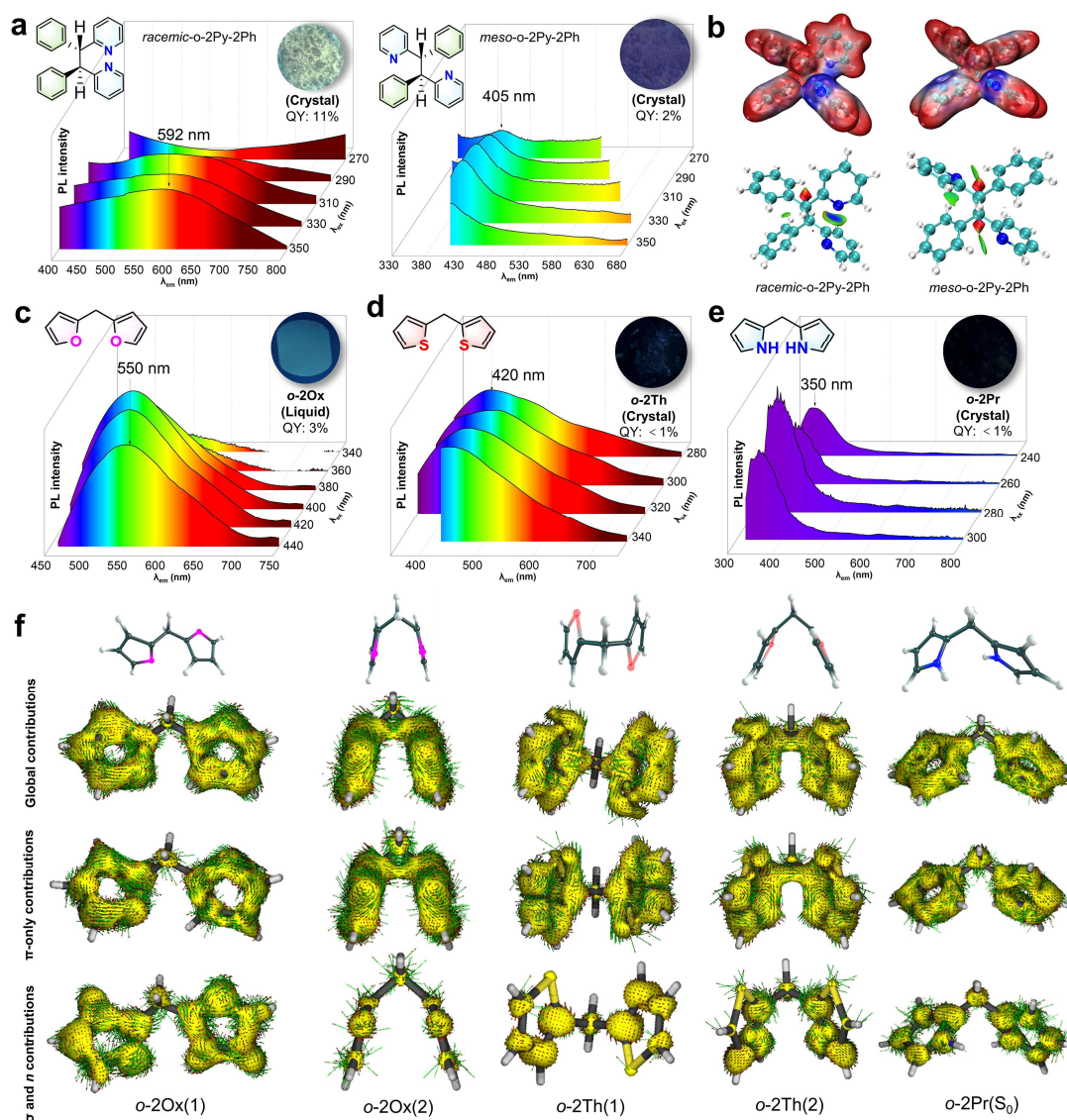
12

Figure 5. Changing the conformations and varying the types of heteroatoms.
(**a**) Excitation-dependent PL spectra of *racemic-o-*2Py-2Ph and *meso-o-*2Py-2Ph (crystalline state).
Their fluorescence pictures are taken under 365 nm. (**b**) ESP and IGMH analysis of *racemic-o-*2Py-2Ph and *meso-o-*2Py-2Ph ($S_{1,min}$). (**c-e**) Excitation-dependent PL spectra of pure (**c**) *o-*2Ox oil, (**d**) *o-*2Th crystal, and (**e**) *o-*2Pr crystal. Their fluorescence pictures are also taken under 365 nm. (**f**) AICD analysis of *o-*2Ox(1), *o-*2Ox(2), *o-*2Th(1) and *o-*2Th(2) conformations. These conformations are obtained by conformational search and TD-DFT calculations. As *o-*2Pr fails conformational convergence in the excited state, its ground-state structure is used for AICD analysis here.

Proof scheme 3: Changing the type of heteroatom in diarylmethane (DAM)

According to the feedback from the database, TSI is also closely related to the type of heteroatom. TAE can be viewed as a superposition of two diarylmethane (DAM) subunits. Thus, to confirm the universality of our TSI database, different heteroatoms were introduced into the DAM. The absorption spectra of *o-*2Ox, *o-*2Th, and *o-*2Pr in ACN exhibit the λ_{ab} at ~235 nm corresponding to the isolated heterocyclic ring, indicating the non-conjugated nature (Figures S56a-c). However, only concentrated solutions of *o-*2Ox show the additional λ_{ab} at 275/328 nm. This is consistent with the

13

excitation tendency of pure compounds, the λ_{ex} of the *o*-2ox compound (420 nm) is the largest (Figures S56d-f). Figure S57 shows PL spectra of them in ACN (1×10^{-5} M) with different λ_{ex}, only showing the emission of the isolated heterocyclic ring (~310 nm).[37] Meanwhile, Figures 5c-5e show PL spectra of *o*-2Ox, *o*-2Th, and *o*-2Pr with different λ_{ex}, which exhibit distinct TSI-induced long-wavelength emissions. At room temperature, *o*-2Ox is liquid, while the other two are crystals. It is known that the oxygen atom in furan can provide a lone pair, although this ability is weaker than the nitrogen atom in pyridine. The furan ring possesses a certain ability to rotate due to a flexible liquid environment, and it can exhibit TSI-induced long-wavelength emission (~550 nm, and QY = 3%) with a certain excitation dependence in Figure 5c. However, *o*-2Th and *o*-2Pr can only exhibit π-π TSI because lone pairs are not involved. Thus, their crystals only show emission peaks of 420 and 350 nm (QY <1%), respectively.

AICD isosurfaces are reused to characterize TSI in Figure 5f. Obvious electron delocalization occurs near the oxygen atoms (according to sigma and *n* contributions), suggesting that significant π/*n*-π TSI exists in *o*-2Ox(1) according to the thickness of the AICD isosurface. Because of the directional nature of the lone pairs, *o*-2Ox(2) cannot form sigma-type *n*-*n* TSI to induce the emission peak beyond 600 nm. Meanwhile, *o*-2Th(1), *o*-2Th(2), and *o*-2Pr can only display π-π TSI due to the absence of lone pairs in Th and Pr. Since the orientation of heteroatoms has little impact on π-π TSI, this elucidates the absence of excitation dependence for the TSI-induced emissions of *o*-2Th and *o*-2Pr crystals.

Proof scheme 4: Increasing the number of heteroatoms to induce *n*-*n* TSI

TSI databases predicted that a larger number of heteroatoms would increase the probability of inducing long-wavelength emission. Hence, we have designed three non-conjugated emitters (*o*-1Py-1Ph, *o*-2Py, and *o*-2Md) with different numbers of N atoms to validate this prediction. In Figures 6a and 6b, excitation-dependent spectra of *o*-1Py-1Ph and *o*-2Py dilute solutions (1×10^{-5} M in ACN) show that their emissions fall in the range of 405~534 nm and 442~534 nm, respectively. This phenomenon may originate from the presence of two types of TSI within the molecule (i.e., *n*/π-π TSI), and the long-wavelength emission peak (~534 nm) may come from *n*-π TSI. However, as the number of N atoms increases, Figure 6c shows that the *o*-2Md dilute solution demonstrates two emissions (534 and 660 nm) without excitation dependence. This incredible red emission may be derived from *n*-*n* TSI, proving that *n*-*n* TSI can stabilize the electronic structure of molecules even in dilute solutions. *o*-1Py-1Ph, *o*-2Py, and *o*-2Md compounds are oily at room temperature, and their heterocyclic rings can rotate actually. However, no matter how the heterocyclic ring rotates, only *n*/π-π TSI could be formed in *o*-1Py-1Ph oil. Thus, the emission spectrum and the corresponding chromaticity (CIE) diagram in Figure 6d demonstrate the single emission peak of 534 nm (QY = 4%). Due to the limited contribution of π-π TSI to long-wavelength emission (beyond 500 nm), this green emission can be attributed to the stable *n*-π TSI in the aggregate state. In Figure 6e, it is worth noting that the spectrum of *o*-2Py exhibits excitation dependence, ranging from 580 to 612 nm (QY = 6%) under different λ_{ex}. This change comes from the formation of additional TSI (i.e., *n*-*n* TSI), and the λ_{em} of 612 nm proves that the luminescence of *o*-4Py crystal (610 nm) could be attributed to one of the pairs of heteroatoms. Its CIE diagram vividly illustrates the redshift of the coordinates (shift to (0.56, 0.44)) resulting from the formation of this new *n*-*n* TSI in DAM. For *o*-2Md, it is conceivable that when pyrimidine possesses the lone pair on both sides, the induction of *n*-*n*/π TSI becomes easier and more efficient compared with *o*-2Py. Therefore, in Figure 6f

14

(Figures S58 and S59), *o*-2Md can demonstrate strong emissions without excitation dependence at both 560 (QY = 7%) and 700 nm (QY = 25%). Based on the aforementioned discussion, the former can be attributed to *n*-π TSI and the latter to *n*-*n* TSI. The CIE coordinate (0.69, 0.31) is almost constant under different λ_{ex}, showing that *o*-2Md is less affected by conformational effects due to the presence of two nitrogen atoms on both sides. Moreover, the intensity of the NIR emission was enhanced by decreasing the temperature from 297 K to 77 K (Figure S60). Notably, a shoulder peak around 750 nm was induced at low temperatures due to the formation of a stronger *n*-*n* TSI. The interference of free radicals for red and NIR emissions based on *n*-*n* TSI was eliminated via the electron spin resonance characterization (Figure S61). At the same time, it is confirmed that these TSI-induced long-wavelength emissions are fluorescence (Figure S62).

We conducted NTO, IGMH, and AICD isosurfaces analyses again based on the conformations obtained through rigorous conformational searching (i.e., *o*-1Py-1Ph, *o*-2Py(1), *o*-2Py(2), *o*-2Md(1) and *o*-2Md(2)). It is found that the above experimental observations closely match the theoretical computational results. Specifically, NTOs show an obvious orbital distribution between adjacent two N atoms in *o*-2Py(2) and *o*-2Md(2), and IGMH analysis demonstrates the different types of TSI in *o*-2Py(2), *o*-2Md(1), and *o*-2Md(2). Thus, there is a clear presence of *n*-*n* TSI in *o*-2Py(2) and *o*-2Md(2), while *n*-π TSI is present in *o*-2Md(1) (Figure S63a and S63b). Meanwhile, by analyzing the shape and thickness of AICD isosurfaces of *o*-2Py(2) and *o*-2Md(2), we demonstrated the presence of distinct sigma-type *n*-*n* TSI within them, which also accounts for the source of their stunning red or NIR emission (Figure S63c).
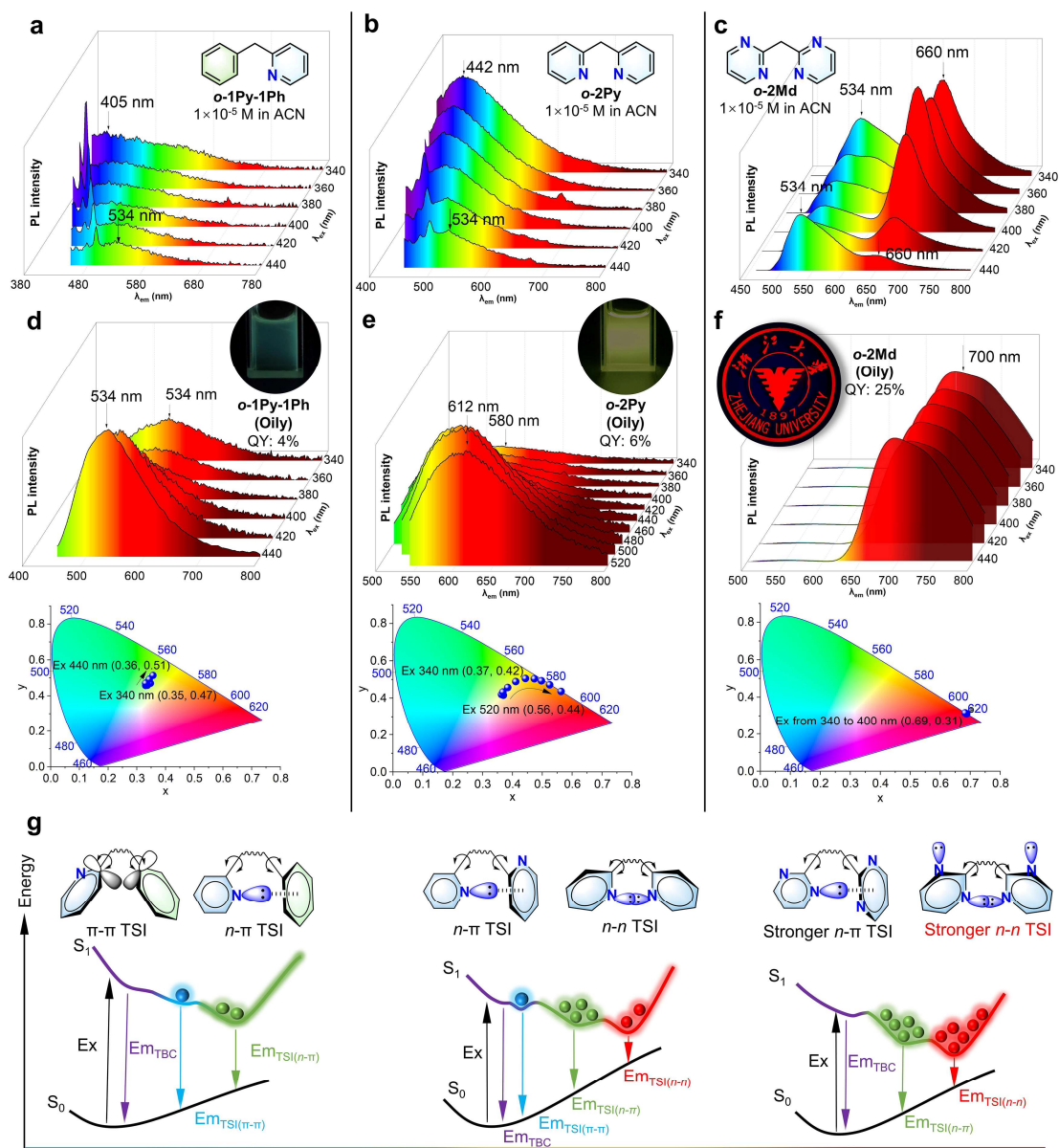
15

Figure 6. Design of ultra-small NIR emitter.
(**a-c**) Excitation-dependent PL spectra of (**a**) *o*-1Py-1Ph, (**b**) *o*-2Py, and (**c**) *o*-2Md in the dilute solutions (1×10⁻⁵ M in ACN). (**d-f**) Excitation-dependent PL spectra and the corresponding CIE diagrams of pure (**d**) *o*-1Py-1Ph (oily liquid), (**e**) *o*-2Py (oily liquid), and (**f**) *o*-2Md (oily liquid). Insets: fluorescence photographs of these pure compounds are taken under 365 nm excitation. (**g**) Three research models show different luminescence mechanisms based on different types and strengths of TSI (i.e., π-π TSI, *n*-π TSI, and *n-n* TSI).

Here, we design the NIR emitter by increasing the number of heteroatoms according to the predicted trend of TSI database. As shown in Figure 6g, different types of TSI will lead to different photophysical mechanisms and properties. For *o*-1Py-1Ph, it can show a weak emission (~405 nm) induced by π-π TSI in the dilute solution and a distinct emission (~534 nm) induced by *n*-π TSI in the aggregate state (oil). Because of the extra nitrogen atom, *o*-2Py is more likely to form *n*-π TSI (~534 nm) compared with *o*-1Py-1Ph at the same conditions. Meanwhile, it is possible for *o*-2Py

16

(oily liquid) to form *n-n* TSI, showing the red emission (~612 nm). For *o*-2Md, the distribution of four lone pairs within such a confined space contributes to the formation of a stronger n-n/π TSI (even in the dilute solution), manifested in the high QY of its oil (up to 25% of 700 nm) and the lack of excitation dependence of these emissions. The increasing trend in QY (from *o*-1Py-1Ph and *o*-2Py to *o*-2Md) demonstrates that sigma-type *n-n* TSI can stabilize the electronic structure, consistent with the above AIMD analysis. Thus, sigma-type *n-n* TSI has been shown as an effective means to attain ultra-small NIR emitters with high performance, and this method is far superior and more efficient than designing large through-bond conjugated emitters (more than 100 atoms). Meanwhile, using various TSIs with different strengths, we declare that full-color ultra-small emitters with non-conjugated structures can be achieved here (Figure S64).

CONCLUSION

Establishing a quantitative relationship between TSI and emission properties through this database has provided valuable insights. Experimental and calculational investigations on various compounds have confirmed the nature of sigma-type *n-n* TSI and its pivotal role in enhancing PL performances. We verify the tendency reflected in the database through four sets of emitters, focusing on the effects of the substituted positions of heteroatoms, the distances between heteroatoms, the types of heteroatoms, and their quantities. Moreover, by concentrating N atoms and enhancing the *n-n* TSI, we have developed an ultra-small NIR emitter of *o*-2Md with only two isolated hexatomic rings, emitting at a wavelength beyond 800 nm and exhibiting a high quantum yield of 25%. Notably, *o*-2Md stands out as the smallest organic NIR emitter known to date. This achievement underscores the significance of sigma-type *n-n* TSI, providing a promising avenue for the design of highly efficient and long-wavelength emitters. Undoubtedly, our work has advanced the understanding of TSI-driven characteristics in molecular systems through the construction of a TSI database, facilitating the development of advanced materials in the field of optoelectronics.

EXPERIMENTAL PROCEDURES

Resource availability

Lead contact
Further information and requests for resources should be directed to and will be fulfilled by the lead contact, H. Zhang (zhanghaoke@zju.edu.cn).

Materials availability
Full experimental details and characterizations can be found in the Supplemental Information. The output files of the calculations have been uploaded. Compounds generated in this study are available upon request to the authors for academic purposes.

Data and code availability
All data supporting this study are available in the manuscript, Supplemental Information, Cambridge Structure Database. The X-ray crystallographic coordinates for structures reported in this work have been deposited at the Cambridge Crystallographic Data Centre (CCDC) under deposition numbers of 2304603 (*p*-4Py) and 2304601 (*o*-4Py). These data can be obtained free of

charge from The Cambridge Crystallographic Data Centre via www.ccdc.cam.ac.uk/data_request/cif.

Chemicals and Materials

The chemicals and reagents used in the experiments were obtained from commercial sources such as Bide Pharmatech Ltd., Energy Chemical, and TCI. Pd/C (10%, dry) was bought from ThermoFisher. The final products were purified multiple times through silica gel column and recrystallization. The purification of all samples was verified by high-performance liquid chromatography (HPLC). The solutions utilized for photophysical measurements were also checked using HPLC.

Calculation methods

The detailed conformational search process can be found in the Supplementary Information.
We employed DFT and TD-DFT calculations using 6-31G(d,p) basis set, B3LYP-D3(BJ). All conformations were simulated in the gas phase. AIMD simulations were conducted using the ORCA 5.0.1 code at the B97-3c level. More details can be found in the Supplementary Information. The names of some used software are OpenBabel 3.1.1,[38] XTB 6.5.0, Molclus 1.12,[39] AICD 2.0,[40] VMD,[41] Multiwfn 3.8,[42] and ORCA 5.0.1.[43]

SUPPLEMENTAL INFORMATION

Supplemental Information includes synthesis of materials, characterization details, somputational details, structural sharacterizations, 65 supplemental figures, and 3 tables can be found with this article online at http:
Video S1-S4 are molecular dynamics trajectories in the excited state based on AIMD analysis. Video S5 is a schematic animation of virtual screening for an ultra-small NIR emitter (made by CINEMA 4D).
The output files of the conformational search and the results of the final TD-DFT calculations have also been uploaded. ("crest_ensemble.xyz", "cluster.xyz" and "S1.mol2")

ACKNOWLEDGMENTS

AUTHOR CONTRIBUTIONS

Z.X. and H.Z. designed the experiments. Z.X. performed the theoretical calculations, synthesis, and photophysical measurements. Z.X., J.Z., L.W., X.L., J.Z.S., H.Z., and B.Z.T. took part in the discussion and gave important suggestions. Z.X. and H.Z. co-wrote the paper. All authors approved the final version of the manuscript.

Reference

1. Shih, W. M. (2015). Exploiting weak interactions in DNA self-assembly. Science *347*, 1417-1418.

2. Nel, A. E., Mädler, L., Velegol, D., Xia, T., Hoek, E. M. V., Somasundaran, P., Klaessig, F., Castranova, V. and Thompson, M. (2009). Understanding biophysicochemical interactions at the nano–bio interface. Nature Mater. *8*, 543–557.

3. Neel, A. J., Hilton, M. J., Sigman, M. S. and Toste, F. D. (2017). Exploiting non-covalent π interactions for catalyst design. Nature *543*, 637-646.

4. Strassfeld, D. A., Chen, C. Y., Park, H. S., Phan, D. Q. and Yu, J. Q. (2023). Hydrogen-bond-acceptor ligands enable distal $C(sp_3)$–H arylation of free alcohols. Nature *622*, 80-86.

5. Hoffmann, R. (1971). Interaction of orbitals through space and through bonds. Acc. Chem. Res. *4*, 1-9.

6. Hierso, J.-C. (2014). Indirect Nonbonded Nuclear Spin–Spin Coupling: A Guide for the Recognition and Understanding of "Through-Space" NMR J Constants in Small Organic, Organometallic, and Coordination Compounds. Chem. Rev. *114*, 4838-4867.

7. Zhen, S., Shen, P., Li, J., Zhao, Z., and Tang, B.Z. (2021). Giant single-molecule conductance enhancement achieved by strengthening through-space conjugation with thienyls. Cell Rep. Phys. Sci. *2*, 100364.

8. Zhang, H., Zheng, X., Xie, N., He, Z., Liu, J., Leung, N. L. C., Niu, Y., Huang, X., Wong, K. S., Kwok, R. T. K., Sung, H. H. Y., Williams, I. D., Qin, A., Lam, J. W. Y., Tang, B. Z. (2017). Why do simple molecules with "isolated" phenyl rings emit visible light? J. Am. Chem. Soc. *139*, 16264−16272.

9. Zhang, H., Zhao, Z., McGonigal, P.R., Ye, R., Liu, S., Lam, J.W.Y., Kwok, R.T.K., Yuan, W.Z., Xie, J., Rogach, A.L.*,* and Tang, B. Z. (2020). Clusterization-triggered emission: Uncommon luminescence from common materials. Mater. Today *32*, 275-292.

10. Tang, S., Yang, T., Zhao, Z., Zhu, T., Zhang, Q., Hou W. and Yuan, W. Z. (2021). Nonconventional luminophores: characteristics, advancements and perspectives. Chem. Soc. Rev. *50*, 12616-12655.

11. Zhang, J., Hu, L., Zhang, K., Liu, J., Li, X., Wang, H., Wang, Z., Sung, H.H.Y., Williams, I.D., Zeng, Z.*,* Lam, J. W. Y., Zhang, H., and Tang, B. Z. (2021). How to manipulate through-space conjugation and clusteroluminescence of simple AIEgens with isolated phenyl rings. J. Am. Chem. Soc. *143*, 9565-9574.

12. Xiong, Z., Zhang, J., Sun, J. Z., Zhang, H. and Tang, B. Z. (2023). Excited-state odd–even effect in through-space interactions. J. Am. Chem. Soc. *145*, 21104-21113.

13. Wang, L., Xiong, Z., Sun, J., Huang, F., Zhang, H., Tang, B. Z. (2024). How the length of through-space conjugation influences the clusteroluminescence of oligo(phenylene methylene)s. Angew. Chem. Int. Ed. *63*, e202318245.

14. Liu, K., Han, P., Yu, S., Wu, X., Tian, Y., Liu, Q., Wang, J., Zhang, M., and Zhao, C. (2022). Hydrogen-Bonding-Induced Clusteroluminescence and UCST-Type Thermoresponsiveness of Nonconjugated Copolymers. Macromolecules *55*, 8599-8608.

15. Liu, P., Fu, W., Verwilst, P., Won, M., Shin, J., Cai, Z., Tong, B., Shi, J., Dong, Y., and Kim, J.S. (2020). MDM2-Associated Clusterization-Triggered Emission and Apoptosis Induction Effectuated by a Theranostic Spiropolymer. *Angew. Chem. Int. Ed. 59*, 8435-8439.

16. Chu, B., Zhang, H., Chen, K., Liu, B., Yu, Q.-L., Zhang, C.-J., Sun, J., Yang, Q., Zhang, X.-H., and Tang, B.Z. (2022). Aliphatic Polyesters with White-Light Clusteroluminescence. J. Am. Chem. Soc. *144*, 15286-15294.

17. Ji, X., Tian, W., Jin, K., Diao, H., Huang, X., Song, G., and Zhang, J. (2022). Anionic polymerization of nonaromatic maleimide to achieve full-color nonconventional luminescence. Nat. Commun. *13*, 3717.

18. Chen, X., Hu, C., Wang, Y., Li, T., Jiang, J., Huang, J., Wang, S., Dong, W., and Qiao, J. (2024). A Self-Assemble Supramolecular Film with Humidity Visualization Enabled by Clusteroluminescence. Adv. Sci. *11*, 2304946.

19. Ye, S., Meftahi, N., Lyskov, I., Tian, T., Whitfield, R., Kumar, S., Christofferson, A. J., Winkler, D. A., Shih, C., Russo, S., Leroux, J., Bao, Y. (2023). Machine learning-assisted exploration of a versatile polymer platform with charge transfer-dependent full-color emission. Chem *9*, 924-947.

20. Du, X., Zhao, S., Wang, L., Wu, H., Ye, F., Xue, K., Peng, S., Xia, J., Sang, Z., Zhang, D., Xiong, Z., Zheng, Z., Xu, L., Niu, G., Tang, J. (2024). Efficient and ultrafast organic scintillators by hot exciton manipulation. Nat. Photon. *18*, 162–169.

21. Gu, L., Shi, H., Bian, L., Gu, M., Ling, K., Wang, X., Ma, H., Cai, S., Ning, W., Fu, L., Wang, H., Wang, S., Gao, Y., Yao, W., Huo, F., Tao, Y., An, Z., Liu, X., Huang, W. (2019). Color-tunable ultralong organic phosphorescence of a single-component molecular crystal. Nat. Photon. *13*, 406-411.

22. Chu, B., Liu, X., Xiong, Z., Zhang, Z., Zhang, C., Sun, J., Zhang, H., Tang, B. Z., Zhang, X. (2024). Enabling nonconjugated polyesters emit full-spectrum fluorescence from blue to near-infrared. Nat. Commun. *15*, 366.

23. Xiong, Z., Zhang, J., Wang, L., Xie, Y., Wang, Y., Zhao, Z., Zhang, H., Sun, J. Z., Huang, F., Tang, B. Z. (2023). Controllable secondary through-space interaction and clusteroluminescence. CCS Chem. *5*, 2832-2844.

24. Horton, M. K., Dwaraknath, S., Persson, K. A. (2021). Promises and perils of computational materials databases. Nat. Comput. Sci. *1*, 3–5.

25. Gómez-Bombarelli, R., Aguilera-Iparraguirre, J., Hirzel, T., Duvenaud, D., Maclaurin, D., Blood-Forsythe, M., Chae, H., Einzinger, M., Ha, D., Wu, T., Markopoulos, G., Jeon, S., Kang, H., Miyazaki, H., Numata, M., Kim, S., Huang, W., Hong, S., Baldo, M. and Adams, R. (2016). Design of efficient molecular organic light-emitting diodes by a high-throughput virtual screening and experimental approach. Nature Mater. *15*, 1120–1127.

26. Song, B., Zhang, J., Zhou, J., Qin, A., Lam, J. & Tang, B. Z. (2023). Facile conversion of water to functional molecules and cross-linked polymeric films with efficient clusteroluminescence. Nat. Commun. *14*, 3115.

27. Pun, S. H., Cheung, K. M., Yang, D., Chen, H., Wang, Y., Kershaw, S. V. and Miao, Q. (2022). A near-infrared absorbing and emissive quadruple helicene enabled by the Scholl reaction of perylene. Angew. Chem. Int. Ed. *61*, e202113203.

28. Hong, G., Antaris, A. L. and Dai, H. (2017). Near-infrared fluorophores for biomedical imaging. Nat. Biomed. Eng. *1*, 0010.

29. Xie, Y., Liu, W., Deng, W., Wu, H., Wang, W., Si, Y., Zhan, X., Gao, C., Chen, X., Wu, H., Peng, J. and Cao, Y. (2022). Bright short-wavelength infrared organic light-emitting devices. Nat. Photon. 16, 752–761.

30. Liu, J., Zhang, H., Hu, L., Wang, J., Lam, J.W.Y., Blancafort, L., and Tang, B.Z. (2022). Through-Space Interaction of Tetraphenylethylene: What, Where, and How. J. Am. Chem. Soc. *144*, 7901-7910.

31. Zhang, Z., Yan, W., Dang, D., Zhang, H., Sun, J.Z., and Tang, B.Z. (2022). The role of amide (n,π∗) transitions in polypeptide clusteroluminescence. Cell Rep. Phys. Sci. *3*, 100716.

32. Li, H.-J., Chen, Y., Wang, H., Wang, H., Liao, Q., Han, S., Li, Y., Wang, D., Li, G., and Deng, Y. (2023). Amide (n, π*) Transitions Enabled Clusteroluminescence in Solid-State Carbon Dots. Adv. Funct. Mater. *33*, 2302862.

33. Liu, M., Han, X., Chen, H., Peng, Q. and Huang, H. (2023). A molecular descriptor of intramolecular noncovalent interaction for regulating optoelectronic properties of organic semiconductors. Nat. Commun. *14*, 2500.

34. Veetil Bijina, P., Suresh, C. H. and Gadre, S. R. (2018). Electrostatics for probing lone pairs and their interactions. J. Comput. Chem. *39*, 488–499.

35. Lu, T., and Chen, Q. (2022). Independent gradient model based on Hirshfeld partition: A new method for visual study of interactions in chemical systems. J. Comput. Chem. *43*, 539–555.

36. Casademont-Reig, I., Woller, T., García, V., Contreras-García, J., Tiznado, W., Torrent-Sucarrat, M., Matito, E., and Alonso, M. (2023). Quest for the Most Aromatic Pathway in Charged Expanded Porphyrins. Chem. Eur. J. *29*, e202202264.

37. Tu, W., Xiong, Z., Zhang, Z., Zhang, J., Wang, L., Xie, Y., Wang, Y., Zhang, H., Sun, J.Z., and Tang, B.Z. (2023). Manipulation of the through-space interactions in diphenylmethane. Smart Mol. *1*, e20220006.

38. Ebejer, J.-P., Morris, G. M., and Deane, C. M. (2012). Freely Available Conformer Generation Methods: How Good Are They? J. Chem. Inf. Model. *52*, 1146–1158.

39. Lu, T., Molclus program, Version 1.12, http://www.keinsci.com/research/molclus.html

40. Geuenich, D., Hess, K., Köhler, F., and Herges, R. (2005). Anisotropy of the Induced Current Density (ACID), a General Method To Quantify and Visualize Electronic Delocalization. Chem. Rev. *105*, 3758-3772.

41. Humphrey, W., Dalke, A., and Schulten, K. (1996). VMD: Visual Molecular Dynamics. J. Mol. Graphics. *14*, 33–38.

42. Lu, T., and Chen, F. (2012). Multiwfn: a Multifunctional Wavefunction Analyzer. J. Comput. Chem. *33*, 580–592.

43. Neese, F. (2022). Software update: The ORCA program system—Version 5.0. WIREs Comput. Mol. Sci. *12*, e1606.